SAGE Publishing

Research Article

Adsorption Characteristics and Electrochemical Behaviors of Methyl Blue onto Magnetic $Mg_xCo_yZn_{(1-x-y)}Fe_2O_4$ Nanoparticles

Zhixiang Lv [ORCID],[1] Xin Yang,[2] Jihong Han,[2] Yingyao Wang,[2] Jiao Zou,[2] Anqi Yang,[2] Haoda Zhang,[2] and Nan He[2]

[1]*The People's Hospital of Danyang, Affiliated Danyang Hospital of Nantong University, Zhenjiang 212300, China*
[2]*School of Pharmacy, Jiangsu University, Zhenjiang 212013, China*

Correspondence should be addressed to Zhixiang Lv; dylvzhixiang@163.com

Magnetic $Mg_xCo_yZn_{(1-x-y)}Fe_2O_4$ nanoparticles were successfully prepared by the rapid combustion approach, and SEM, XRD, VSM, EDX, and FTIR techniques were applied for their characterization. The influence of the element ratios (Mg^{2+}, Co^{2+}, and Zn^{2+}) in magnetic $Mg_xCo_yZn_{(1-x-y)}Fe_2O_4$ nanoparticles on their properties was explored. To acquire a larger specific surface area for better adsorption of methyl blue (MB), magnetic $Mg_{0.4}Co_{0.5}Zn_{0.1}Fe_2O_4$ nanoparticles calcined at 400°C for 2 h with 25 mL anhydrous ethanol were selected, and their average particle size and the saturation magnetization were about 81.3 nm and 13.5 emu·g^{-1}, respectively. Adsorption kinetics models and adsorption isotherm models were applied to research the adsorption characteristics of MB onto magnetic $Mg_{0.4}Co_{0.5}Zn_{0.1}Fe_2O_4$ nanoparticles. The pseudo-second-order kinetics model ($R^2 > 0.99$) and Temkin isotherm model ($R^2 = 0.9887$) were the most consistent with the data, indicating that the adsorption was the chemical multilayer adsorption mechanism, and the process was an exothermic reaction. The E of the Dubinin-Radushkevich (D-R) isotherm model was 0.2347 KJ·mol^{-1}, indicating the adsorption involved physical adsorption besides chemical adsorption. The ΔG^0 and ΔH^0 ($\Delta H^0 = -10.38$ KJ·mol^{-1}) of the adsorption process of MB adsorbed onto magnetic $Mg_{0.4}Co_{0.5}Zn_{0.1}Fe_2O_4$ nanoparticles measured through the thermodynamic experiment were both less than 0, which proved that the process was a spontaneous exothermic reaction. The adsorption capacity of MB onto magnetic $Mg_{0.4}Co_{0.5}Zn_{0.1}Fe_2O_4$ nanoparticles increased with the pH of MB solution increasing from 2 to 4 at room temperature, and it had no significant change when the pH of MB solution was 4-12, while the relative removal rate was 98.75% of the first one after 2 cycles. The electrochemical impedance spectroscopy (EIS) and the cyclic voltammetry (CV) data further demonstrated that MB was adsorbed onto magnetic $Mg_{0.4}Co_{0.5}Zn_{0.1}Fe_2O_4$ nanoparticles.

1. Introduction

Dyes have been widely used in textiles, coatings, paint, plastic, and other industries which make people's lives become colorful [1–6]. Meanwhile, environmental pollution has become increasingly serious owing to the discharge of a great deal of dye wastewater, especially, the nondegradable substances and aromatic and other organics of dyes that make the water eutrophication and absorbed by plants; many of them have serious harm to the environment and eventually enter the human body through the food chain that has a great threat to human health [7–11]. Hence, solving dye pollution has become a serious problem. Many methods of treating dye wastewater have been widely used, such as the membrane separation method [12, 13], photodegradation [14, 15], electrochemical oxidation method [16, 17], and adsorption method [18, 19]. Considering the low cost, no secondary pollution, recycling, and other influence factors, the adsorption method stands out from these methods [20–22].

The adsorbent is a key factor in the adsorption process, and many usual adsorbents, for instance, activated carbon [23], silica gel [24], resin [25], zeolite [26], and activated alumina [27], are applied to treat dye wastewater. With the development of nanotechnology, for larger specific surface area and high adsorption capacity,

nanomaterials are applied for adsorption. Whereas, the difficult separation revealed the disadvantage of nanomaterials for adsorption. To solve the question, magnetic nanomaterials are used for adsorption, and they can be facilely separated from wastewater with an external magnetic field [28–31].

Many approaches can be applied for the preparations of magnetic nanomaterials, such as coprecipitation [32, 33], sol-gel [34], rapid combustion [35], and hydrothermal methods [36]. The coprecipitation method is easy to cause a high local concentration of solution owing to precipitant, leading to agglomeration [37]; and the sol-gel method has the disadvantages of a long preparation cycle and high cost [38], while the hydrothermal method has high requirements on the reaction temperature and pressure and has great safety risks [38]. Compared to these methods, the rapid combustion method has advantages such as low cost, a short preparation period, low equipment requirements, and other advantages.

Spinel ferrites (MFe_2O_4, M=Mg, Co, Zn, Cu, Ni, etc.) are a kind of magnetic nanomaterials which have been widely studied due to their unique magnetic properties and electrical resistances [39–41]. $MgFe_2O_4$, $CoFe_2O_4$, and $ZnFe_2O_4$ are often used as adsorbents. $MgFe_2O_4$ has high adsorption capacity and strong stability. Saturated magnetization and coercivity of $MgFe_2O_4$ could be improved by permeating Co into $MgFe_2O_4$ due to the saturated magnetization of $CoFe_2O_4$ being greater than $MgFe_2O_4$ [42, 43]. The specific surface area ratio of $MgFe_2O_4$ could be increased by permeating Zn into $MgFe_2O_4$ because $ZnFe_2O_4$ has a large specific surface area [44]. Although magnetic $Mg_xCo_yZn_{(1-x-y)}Fe_2O_4$ nanoparticles have some advantages, they have not been widely applied because of their less mature technology.

In this work, magnetic $Mg_xCo_yZn_{(1-x-y)}Fe_2O_4$ nanoparticles were successfully prepared by the rapid combustion approach, and MB was selected as the dye adsorption model which was a complex aromatic and typical anionic dye, the adsorption mechanism of MB onto $Mg_xCo_yZn_{(1-x-y)}Fe_2O_4$ nanoparticles was investigated [1].

2. Experimental Detail

2.1. Materials.
Absolute ethanol, ferric nitrate nonahydrate ($Fe(NO_3)_3 \cdot 9H_2O$, AR), cobalt nitrate hexahydrate ($Co(NO_3)_2 \cdot 6H_2O$, AR), magnesium nitrate hexahydrate ($Mg(NO_3)_2 \cdot 6H_2O$, AR), zinc nitrate hexahydrate ($Zn(NO_3)_2 \cdot 6H_2O$, AR), and methyl blue (MB, BS) were purchased from Sinopharm Chemical Reagent Co., Ltd (Shanghai, China).

2.2. Preparation and Characteristic of Magnetic $Mg_xCo_yZn_{(1-x-y)}Fe_2O_4$ Nanoparticles.
The rapid combustion approach was employed to prepare magnetic $Mg_xCo_yZn_{(1-x-y)}Fe_2O_4$ nanoparticles. At room temperature, $Mg(NO_3)_2 \cdot 6H_2O$, $Co(NO_3)_2 \cdot 6H_2O$, $Zn(NO_3)_2 \cdot 6H_2O$, $Fe(NO_3)_3 \cdot 9H_2O$, and anhydrous ethanol (15 mL, 25 mL, 35 mL, 45 mL, 55 mL, and 100 mL) were added to a beaker according to the design ratio (x : y : (1-x-y) : 2). Then, the beaker was mag-

netically stirred until a homogeneous solution was formed. The homogeneous solution was moved to a crucible for combustion until the flame went out. Then, the crucible was placed in a calcinatory with programmed temperature controlling for calcination and ground after calcination.

The phase identification of magnetic $Mg_xCo_yZn_{(1-x-y)}Fe_2O_4$ nanomaterials was analyzed by X-ray diffraction (XRD, Rigaku D/max 2500 PCX), a vibrating sample magnetometer (VSM, HH-15, Physcience Opto-electronics Co., Ltd., Beijing, China), and the scanning electron microscopy (SEM, JSM-TOOIF, JEOL Ltd., Japan) that were used to investigate their hysteresis loops and morphology, respectively; the energy dispersive spectroscopy (EDS) was selected to analyze the corresponding element composition, and magnetic $Mg_xCo_yZn_{(1-x-y)}Fe_2O_4$ nanoparticles were added to the milled KBr for grinding and analyzing their Fourier transform infrared spectroscopy (FTIR, Nicolet Avatar, America) at 4000 cm^{-1}-400 cm^{-1}.

2.3. Adsorption Experiments of MB onto $Mg_{0.4}Co_{0.5}Zn_{0.1}Fe_2O_4$ Nanoparticles.
To investigate the adsorption kinetics characteristics of MB onto $Mg_{0.4}Co_{0.5}Zn_{0.1}Fe_2O_4$ nanoparticles, each of 5 mg magnetic $Mg_{0.4}Co_{0.5}Zn_{0.1}Fe_2O_4$ nanoparticles was added into 2 mL MB solution (1900-2200 mg·L^{-1}, the gradient of 100 mg·L^{-1}) at room temperature and pH of 4, sonicated for 5 min and stirred for a corresponding time, then centrifuged at 10000 rpm for 5 min. The absorbance of supernatant after centrifugation of magnetic $Mg_{0.4}Co_{0.5}Zn_{0.1}Fe_2O_4$ nanoparticles was measured by ultraviolet spectrophotometer. To research the adsorption relationship of MB and magnetic $Mg_{0.4}Co_{0.5}Zn_{0.1}Fe_2O_4$ nanoparticles, similarly, each 5 mg magnetic $Mg_{0.4}Co_{0.5}Zn_{0.1}Fe_2O_4$ nanoparticles were added into 2 mL MB solution with various initial concentrations of 400-2200 mg·L^{-1} and the gradient of 200 mg·L^{-1} and kept for 24 h. Then, centrifuged and the supernatants were taken for measurements. To investigate the effect of MB solution temperature on the adsorption capacity of magnetic $Mg_{0.4}Co_{0.5}Zn_{0.1}Fe_2O_4$ nanoparticles, the experimental steps of isotherm were repeated at 303 K, 313 K, and 323 K, respectively. To study the effect of pH on the adsorption capacity, 1 M NaOH solution and 1 M hydrochloric acid were used for accommodating the pH of MB solutions (2, 4, 6, 8, 10, and 12), and the adsorption capacities under various pH values were examined under with 2000 mg·L^{-1} of the initial MB solution. To investigate the adsorption reusability of MB onto magnetic $Mg_{0.4}Co_{0.5}Zn_{0.1}Fe_2O_4$ nanoparticles, 100 mg of magnetic $Mg_{0.4}Co_{0.5}Zn_{0.1}Fe_2O_4$ nanoparticles were added to 40 mL MB solution (2000 mg·L^{-1}), and when the adsorption was finished, the magnetic $Mg_{0.4}Co_{0.5}Zn_{0.1}Fe_2O_4$ nanoparticles that adsorbed MB were separated and recalcined again at 400°C for 2 h, and the adsorption was repeated. Formula (1) was employed to calculate the adsorption capacity of $Mg_{0.4}Co_{0.5}Zn_{0.1}Fe_2O_4$ nanoparticles for MB [45].

$$q_t = \frac{(C_0 - C_t) \cdot V}{m}, \tag{1}$$

where C_0 (mg·L^{-1}) and C_t (mg·L^{-1}) were the initial concentration of MB and the concentration after adsorption, respectively.

(a)

(b)

(c)

(d)
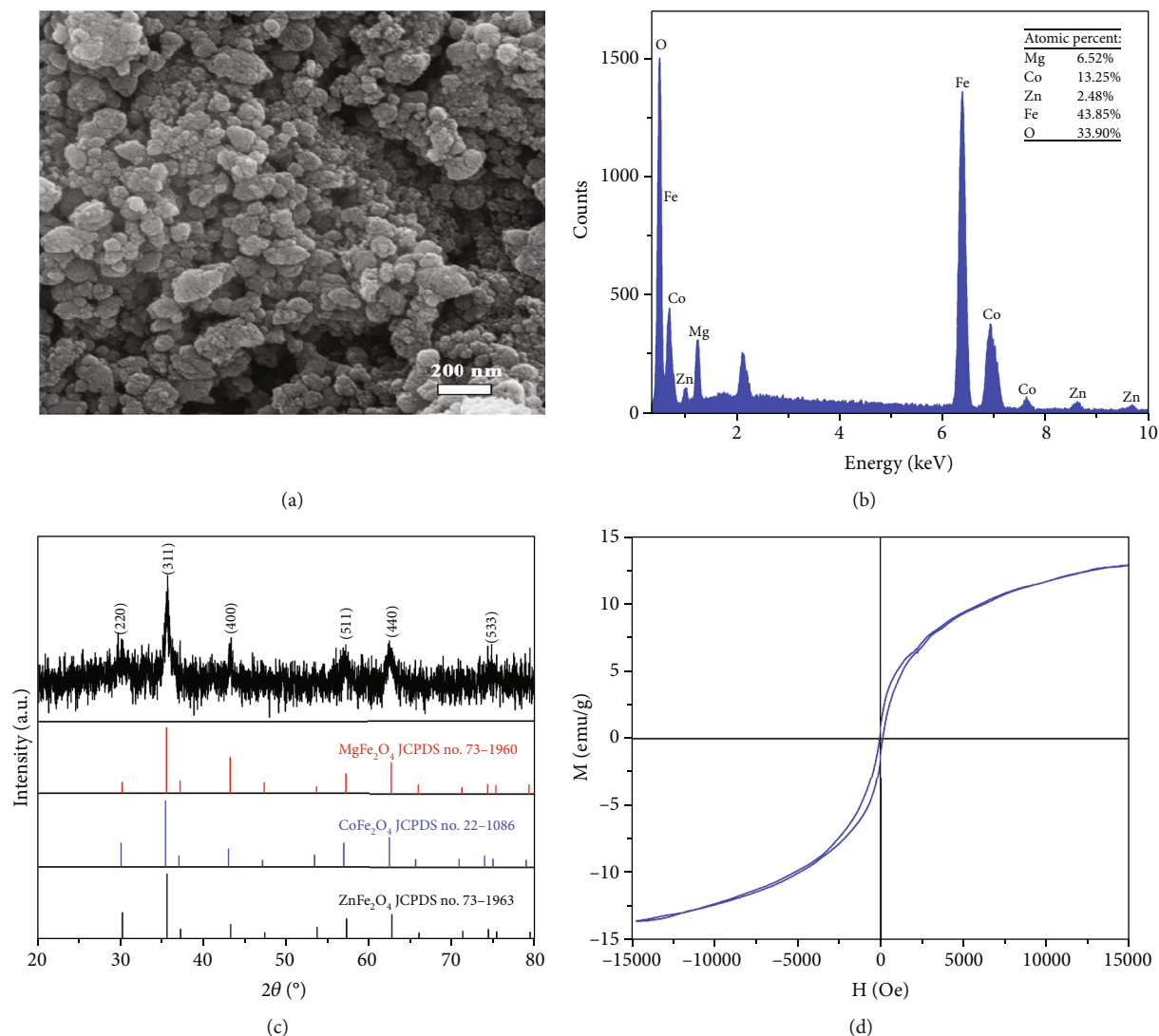
FIGURE 1: The SEM (a), EDS (b), XRD (c), and VSM (d) of magnetic $Mg_{0.4}Co_{0.5}Zn_{0.1}Fe_2O_4$ nanomaterials calcined at 400˚C for 2 h with 25 mL anhydrous ethanol.

m (g) was the weight of magnetic $Mg_{0.4}Co_{0.5}Zn_{0.1}Fe_2O_4$ nanoparticles, and V (L) was the volume of the MB solution.

2.4. Electrochemical Performances of MB onto Magnetic $Mg_{0.4}Co_{0.5}Zn_{0.1}Fe_2O_4$ Nanoparticles. To investigate the electrochemical changes for the adsorption process of MB onto $Mg_{0.4}Co_{0.5}Zn_{0.1}Fe_2O_4$ nanoparticles. At room temperature, 1 mg magnetic $Mg_{0.4}Co_{0.5}Zn_{0.1}Fe_2O_4$ nanoparticles and 1 mg magnetic $Mg_{0.4}Co_{0.5}Zn_{0.1}Fe_2O_4$ nanoparticles adsorbing MB were put into 100 μL ultrapure water to make suspension liquids, then ultrasound for 30 min, respectively. The two suspension liquids mentioned above of 8 μL were sucked and added onto the magnetic glassy carbon electrodes which were ground by alumina, respectively, and then dried to obtain the electrodes to be tested. Then, magnetic glassy carbon electrode, Ag/AgCl electrode, and platinum wire electrode were regarded as the working electrode, the reference electrode, and the counter electrode, respectively; 0.1 M KCl was used as the electrolyte which contained 5 mM $[Fe(CN)_6]^{3-/4-}$.

3. Results and Discussion

3.1. Characterization of Magnetic $Mg_{0.4}Co_{0.5}Zn_{0.1}Fe_2O_4$ Nanomaterials. $Mg_xCo_yZn_{(1-x-y)}Fe_2O_4$ nanomaterials calcined at 400˚C for 2 h with anhydrous ethanol of 25 mL were characterized as displayed in Figure 1. Figure 1(a) revealed the SEM morphology of $Mg_xCo_yZn_{(1-x-y)}Fe_2O_4$ nanomaterials, and the acceleration voltage of SEM was 20 KV, and it was obvious that the $Mg_xCo_yZn_{(1-x-y)}Fe_2O_4$ nanomaterials were spherical particles with the average grain diameter of 81.3 nm. The corresponding EDS spectrogram of $Mg_xCo_yZn_{(1-x-y)}Fe_2O_4$ nanoparticles was displayed in Figure 1(b), and the proportions of all elements were consistent with the hypothesis before the experiment which proved the formation of $Mg_{0.4}Co_{0.5}Zn_{0.1}Fe_2O_4$ nanoparticles. The XRD pattern of $Mg_{0.4}Co_{0.5}Zn_{0.1}Fe_2O_4$ nanoparticles was revealed in Figure 1(c); the peaks corresponded with the standard PDF cards (JCPDS No. 73-1960, JCPDS No. 22-1086, JCPDS No. 73-1963) [46–48]. The cell parameters of $Mg_{0.4}Co_{0.5}Zn_{0.1}Fe_2O_4$ nanoparticles were $a = b = c = 8.3919$ Å, $\alpha = \beta = \gamma = 90 \circ$, and

the volume of 590.99 Å^3, which suggested that $Mg_{0.4}Co_{0.5}Zn_{0.1-}Fe_2O_4$ nanoparticles were cubic type [49]. The hysteresis loops of $Mg_{0.4}Co_{0.5}Zn_{0.1}Fe_2O_4$ nanoparticles were shown in Figure 1(d), and the saturation magnetization (M_s) was 13.5 emu·g^{-1}, which contributed to being separated after adsorption.

3.2. Optimum Preparation Conditions of $Mg_xCo_yZn_{(1-x-y)}Fe_2O_4$ Nanoparticles.

To acquire a larger specific surface area, the element ratios (Mg, Co, and Zn) of magnetic $Mg_xCo_yZn_{(1-x-y)}Fe_2O_4$ nanoparticles were investigated, and their XRD patterns, average grain sizes, and the hysteresis loops of magnetic $Mg_xCo_yZn_{(1-x-y)}Fe_2O_4$ ($x = 0.1$ and $y = 0.1 - 0.8$) nanoparticles were shown in Figure S1(A-C), respectively. The wider and the lower the peak was, the lower the crystallinity was, the smaller the average grain diameter was, the larger the specific surface area of the nanomaterials was, and the better the adsorption efficiency of the nanomaterials was. It was obvious that the peak was the widest when y was 0.5. The average grain size was calculated by the Scheller formula [50] and was 10.8-11.4 nm, and the average grain size was the smallest when y was 0.5. With the increase of Co content and the decrease of Zn content, the saturation magnetization generally presented a rising trend, the reason for which was that the saturation magnetization of $CoFe_2O_4$ was higher than that of $ZnFe_2O_4$ [51]. The XRD patterns, average grain diameter, and the hysteresis loops of magnetic $Mg_xCo_yZn_{(1-x-y)}Fe_2O_4$ ($y = 0.5$ and $x = 0.1 - 0.4$) nanoparticles were revealed in Figure S1(D-F), respectively. It was obvious that the peak was the widest when x was 0.4. The average grain diameter decreased from 10.8 nm ($x = 0.1$) to 10.0 nm ($x = 0.4$), indicating that the average grain diameter of magnetic $Mg_xCo_yZn_{(1-x-y)}Fe_2O_4$ nanoparticles had a strong dependence on the content of Zn. Because the M_s value of $MgFe_2O_4$ was lower than that of $ZnFe_2O_4$, the M_s value of magnetic $Mg_xCo_yZn_{(1-x-y)}Fe_2O_4$ nanoparticles decreased gradually with the increase of Mg content [52]. Hence, the magnetic $Mg_{0.4}Co_{0.5}Zn_{0.1}Fe_2O_4$ nanoparticles with a larger saturation magnetization were selected to investigate the property and employed to adsorb MB.

The influences of anhydrous ethanol volume and calcination temperature on magnetic $Mg_{0.4}Co_{0.5}Zn_{0.1}Fe_2O_4$ nanoparticles were investigated. The XRD patterns, average grain diameter, and the hysteresis loops of magnetic $Mg_{0.4}Co_{0.5}Zn_{0.1}Fe_2O_4$ nanoparticles calcined at different temperatures for 2 h with 25 mL anhydrous ethanol were displayed in Figure S2(A-C), respectively. It was obvious that the peak of the calcination temperature at 400°C was the widest. While, with the calcination temperature increasing from 400°C to 800°C, the diffraction peak intensity of 35.57° gradually increased, and the average grain diameter increased from 10.0 nm to 30.1 nm. The calcination temperature had a larger influence on the average grain size. The reason was that the sintering degree was getting better with the increase in calcination temperature. The M_s value of nanoparticles was related to their average grain diameter. The M_s value increased with
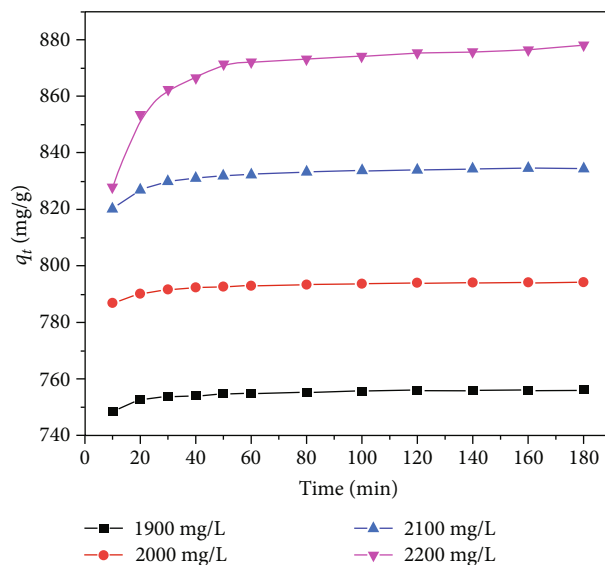

FIGURE 2: Adsorption kinetics curves of MB onto $Mg_{0.4}Co_{0.5}Zn_{0.1}Fe_2O_4$ nanoparticles at the various initial MB concentrations.

the increase of calcination temperature, and the same trend was shown in average particle size. The reason was that magnetic $Mg_{0.4}Co_{0.5}Zn_{0.1}Fe_2O_4$ nanoparticles formed more easily at a higher temperature. The XRD patterns, average grain diameter, and the hysteresis loops of magnetic $Mg_{0.4}Co_{0.5}Zn_{0.1}Fe_2O_4$ nanoparticles prepared at 400°C for 2 h with various dosages of anhydrous ethanol were displayed in Figure S2(D-F), respectively. The average grain size decreased with the dosage of anhydrous ethanol increasing from 15 mL to 25 mL. However, it increased with the dosage of anhydrous ethanol increasing from 25 mL to 100 mL. The reason was that the crystalline grain did not form when the dosage of anhydrous ethanol was 15 mL. And the higher the dosage of anhydrous ethanol was, the better the sintering degree was. The maximum saturation magnetization of magnetic $Mg_{0.4}Co_{0.5}Zn_{0.1}Fe_2O_4$ nanoparticles reached 69.52 emu·g^{-1} when anhydrous ethanol was 45 mL. To adsorb more MB and for easy separation, after comprehensive consideration, the calcination temperature of 400°C and the absolute ethanol dosage of 25 mL were the best optimums for preparing magnetic $Mg_{0.4}Co_{0.5}Zn_{0.1}Fe_2O_4$ nanoparticles.

3.3. Adsorption Characteristics of MB onto $Mg_{0.4}Co_{0.5}Zn_{0.1}Fe_2O_4$ Nanoparticles

3.3.1. Adsorption Kinetics.
The relationships between different initial concentrations of MB solution and the adsorption capacities of magnetic $Mg_{0.4}Co_{0.5}Zn_{0.1}Fe_2O_4$ nanoparticles were shown in Figure 2; the adsorption capacity of magnetic $Mg_{0.4}Co_{0.5}Zn_{0.1}Fe_2O_4$ nanoparticles for MB increased gradually with the increase of initial MB concentration. The reason was that the adsorption sites of magnetic $Mg_{0.4}Co_{0.5}Zn_{0.1}Fe_2O_4$ nanoparticles were much more than the required adsorption sites of MB in the solution with
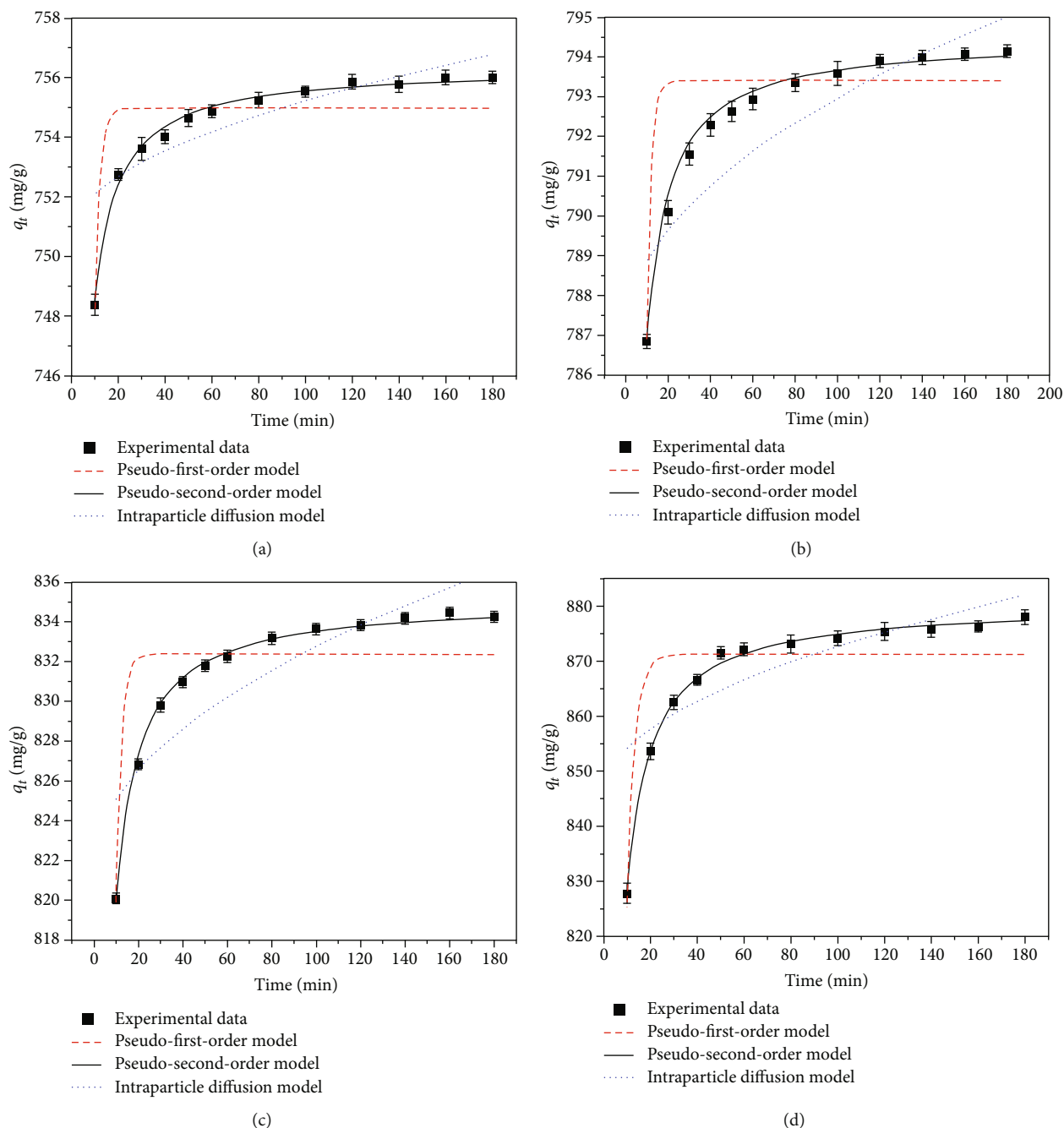
(a)

(b)

(c)

(d)

FIGURE 3: The pseudo-first-order, pseudo-second-order, and intraparticle models of MB onto $Mg_{0.4}Co_{0.5}Zn_{0.1}Fe_2O_4$ nanoparticles with an initial MB concentration of 1900 mg·L^{-1} (a), 2000 mg·L^{-1} (b), 2100 mg·L^{-1} (c), and 2200 mg·L^{-1} (d).

the low initial concentration of MB, and MB was adsorbed onto magnetic $Mg_{0.4}Co_{0.5}Zn_{0.1}Fe_2O_4$ nanoparticles and reached saturation soon. And the required adsorption sites of MB augmented with the increase of initial MB concentration; most of the adsorption sites of magnetic $Mg_{0.4}Co_{0.5}Zn_{0.1}Fe_2O_4$ nanoparticles were rapidly occupied by MB, and the adsorption rate gradually decreased. Magnetic $Mg_{0.4}Co_{0.5}Zn_{0.1}Fe_2O_4$ nanoparticles had a large number of effective adsorption sites in a short adsorption time. With the extension of the adsorption time, the effective adsorption sites decreased, and the adsorption rate gradu-

ally decreased until it stabilized, which reached the maximum saturated adsorption capacity.

Three frequently used kinetics models, pseudo-first-order, pseudo-second-order, and intraparticle models [53–55], were applied to investigate the adsorption process of MB onto magnetic $Mg_{0.4}Co_{0.5}Zn_{0.1}Fe_2O_4$ nanoparticles. Equations (2)–(4) of the pseudo-first-order model, pseudo-second-order model, and intraparticle model were as follows:

$$q_t = q_e\left(1 - e^{-k_1 t}\right), \qquad (2)$$

Table 1: Fitted kinetics parameters for adsorptions of MB in aqueous solution onto $Mg_{0.4}Co_{0.5}Zn_{0.1}Fe_2O_4$ nanoparticles at room temperature.

Kinetics models	Equations	Parameters	Initial concentration of MB (mg·L^{-1})			
			1900	2000	2100	2200
Pseudo-first-order model	$q_t = q_e\left(1 - e^{-k_1 t}\right)$	q_e	754.9470	792.9734	832.3179	871.1886
		k_1	0.4740	0.48560	0.4208	0.2963
		R^2	0.7752	0.6888	0.7231	0.7961
Pseudo-second-order model	$q_t = q_e^2 k_2 t / 1 + q_e k_2 t$	q_e	756.3431	794.3882	835.0674	880.4483
		k_2	0.0125	0.0126	0.0064	0.0018
		R^2	0.9927	0.9911	0.9964	0.9966
Intraparticle diffusion model	$q_t = x_i + k_i t^{1/2}$	x_i	749.7993	787.7387	822.2724	837.7911
		k_i	0.5401	0.5546	1.0581	3.4625
		R^2	0.6983	0.7482	0.7158	0.6591

q_e (mg·g^{-1}) and q_t (mg·g^{-1}) were the amounts of MB adsorbed at equilibrium and at any time (t), respectively; k_1 (min^{-1}), k_2 (mg·g^{-1}·min^{-1}), and k_i (mg·g^{-1}·min^{-1}) were the adsorption rate constants for the corresponding model; x_i was the constants of the intraparticle diffusion model.

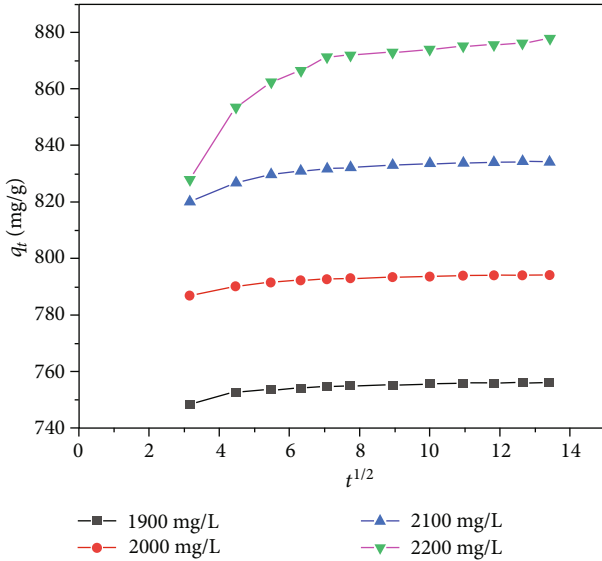Figure 4: Intraparticle diffusion kinetic plots for MB adsorption onto $Mg_{0.4}Co_{0.5}Zn_{0.1}Fe_2O_4$.

Figure 5: Adsorption isotherms of MB onto $Mg_{0.4}Co_{0.5}Zn_{0.1}Fe_2O_4$ nanoparticles at room temperature.

$$q_t = \frac{q_e^2 k_2 t}{1 + q_e k_2 t}, \qquad (3)$$

$$q_t = x_i + k_i t^{1/2}, \qquad (4)$$

where q_t (mg·g^{-1}) and q_e (mg·g^{-1}) were the adsorption capacity of MB adsorbed onto magnetic $Mg_{0.4}Co_{0.5}Zn_{0.1}Fe_2O_4$ nanoparticles at t time and equilibrium time, respectively. k_1, k_2, and k_i were the rate constants of pseudo-first-order model, pseudo-second-order model, and intraparticle model, respectively. x_i was the thickness of the adsorbed boundary layer. The kinetics fitting curves of magnetic $Mg_{0.4}Co_{0.5}Zn_{0.1}Fe_2O_4$ nanoparticles with various initial concentrations of MB and different adsorption times were shown in Figure 3. Obviously, the experimental data conformed to the pseudo-second-order kinetics model. The closer the correlation coef-
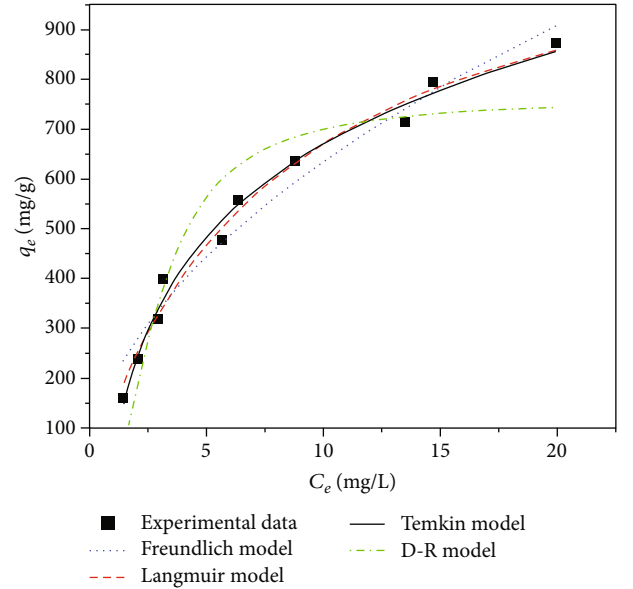
ficient (R^2) was to 1, the more consistent the fitting curve was with the experimental data. Table 1 reveals that the R^2 values of pseudo-second-order kinetics models were greater than 0.99, indicating that the adsorption of MB onto magnetic $Mg_{0.4}Co_{0.5}Zn_{0.1}Fe_2O_4$ nanoparticles was chemical adsorption. The chemisorption mechanism might affect its adsorption rate due to electron transfer between adsorbents and adsorbates [56].

The rate-limiting steps of methyl blue adsorption on nanoparticles were determined by the intraparticle diffusion model. As could be seen from Figure 4, the curve presented multilinearity and did not pass through the origin, indicating that intraparticle diffusion was not the only rate-limiting step. The adsorption process of MB onto $Mg_{0.4}Co_{0.5}Zn_{0.1}Fe_2O_4$ was roughly divided into three stages.

TABLE 2: The parameter values for Langmuir, Freundlich, Temkin, and D-R models for MB onto $Mg_{0.4}Co_{0.5}Zn_{0.1}Fe_2O_4$ nanoparticles at room temperature.

Model	Equation	R^2	Adj. R^2	Parameters	Estimated value
Langmuir	$q_e = q_{max}K_LC_e/1 + K_LC_e$	0.9859	0.9841	q_{max}	1192.3575
				K_L	0.1287
Freundlich	$q_e = K_FC_e^{1/n}$	0.9665	0.9623	K_F	192.5846
				$1/n$	0.5182
Temkin	$q_e = Bln(A_TC_e)$	0.9887	0.9873	B	268.8678
				A_T	1.2038
D-R	$q_e = q_{max}e^{-\beta[RTln(1+1/Ce)]^2}$ $E = \sqrt{1/2\beta}$	0.8929	0.8795	q_{max}	759.5958
				β	9.0796
				E	0.2347

q_{max} was the maximum adsorption capacity of MB onto magnetic $Mg_{0.4}Co_{0.5}Zn_{0.1}Fe_2O_4$ nanoparticles; K_L, K_F, and $1/n$ were constants for the corresponding model.

TABLE 3: Comparison of the maximum adsorption capacities of MB onto $Mg_{0.4}Co_{0.5}Zn_{0.1}Fe_2O_4$ nanoparticles with other adsorbents.

Adsorbents	Dose (mg·mL^{-1})	Temperature (°C)	q_{max} (mg·g^{-1})	References
SNCs-PEI	1	25	337.84	[35]
GO-CS aerogel	0.8	25	110.9	[71]
CNF/P-70 aerogel	0.5	25	598.8	[72]
TPP-PP	0.5	25	160.01	[73]
GO	0.01	30	419.5295	[74]
APG	0.01	30	821.05	[74]
$Mg_{0.4}Co_{0.5}Zn_{0.1}Fe_2O_4$ nanoparticles	2.5	RT	1162.3431	This work

The first stage was the surface adsorption process of $Mg_{0.4}Co_{0.5}Zn_{0.1}Fe_2O_4$ nanoparticles, namely, MB diffusion adsorption on the surface of $Mg_{0.4}Co_{0.5}Zn_{0.1}Fe_2O_4$ nanoparticles. The second stage was the diffusion process within the $Mg_{0.4}Co_{0.5}Zn_{0.1}Fe_2O_4$ nanoparticle, which was the process of MB diffusion into the nanoparticles, and the third stage was the process of slow adsorption to adsorption equilibrium. The results showed that the control steps of the adsorption process of MB onto $Mg_{0.4}Co_{0.5}Zn_{0.1}Fe_2O_4$ were carried out through the coupling of external diffusion and internal diffusion [57–59].

3.3.2. Adsorption Isotherms. The adsorption isotherm was used to investigate the interaction between MB and magnetic $Mg_{0.4}Co_{0.5}Zn_{0.1}Fe_2O_4$ nanoparticles. The experimental data were fitted with the Langmuir model, Freundlich model, Temkin model, and D-R model, respectively, as displayed in Figure 5. The Langmuir model assumed that monolayer adsorption on uniformly distributed adsorbent at active sites [60]. The Freundlich model assumed that multilayer adsorption was performed on heterogeneous surfaces [61]. The Temkin model assumed that monolayer and multilayer adsorption was performed on heterogeneous surfaces [62]. The D-R model assumed that adsorption was related to surface porosity and pore volume. D-R isotherm models examined adsorption in terms of energy to determine physical or chemisorption processes [63]. Equations (5)–(9) of

the isotherms were as follows:

$$q_e = \frac{q_{max}K_LC_e}{1 + K_LC_e}, \tag{5}$$

$$q_e = K_FC_e^{1/n}, \tag{6}$$

$$q_e = Bln(A_TC_e), \tag{7}$$

$$q_e = q_{max}e^{-\beta\left[RTln\left(1+\frac{1}{C_e}\right)\right]^2}, \tag{8}$$

$$E = \sqrt{\frac{1}{2\beta}}, \tag{9}$$

where q_e (mg·g^{-1}) and q_{max} (mg·g^{-1}) were the adsorption equilibrium capacity and maximum adsorption capacity of MB adsorbed onto magnetic $Mg_{0.4}Co_{0.5}Zn_{0.1}Fe_2O_4$ nanoparticles, respectively. C_e (mg·L^{-1}) was the equilibrium concentration. K_F and K_L were the rate constant of the Langmuir model and Freundlich model, respectively. A_T and B were constants of the Temkin isotherm model. β was a constant related to the adsorption energy, and E (KJ·mol^{-1}) was the mean adsorption energy. The relevant parameters of the isotherm models were listed in Table 2. The correlation coefficients (R^2) of the Langmuir model, Freundlich model, and Temkin model were 0.9859, 0.9665, and 0.9887, respectively, and the R^2 of the Temkin model was greater than that of the

Langmuir and Freundlich models, indicating that the Temkin model was fitter for explaining the adsorption relationship between MB and magnetic $Mg_{0.4}Co_{0.5}Zn_{0.1}Fe_2O_4$ nanoparticles. The adsorption of MB onto magnetic $Mg_{0.4}Co_{0.5}Zn_{0.1}Fe_2O_4$ nanoparticles was a monolayer and multilayer chemical adsorption mechanism. Moreover, B of the Temkin model was positive, indicating that the adsorption was an exothermic reaction [64–66].

D-R isothermal model was employed to calculate the average adsorption energy. When $E < 8$ KJ·mol^{-1}, the physical adsorption occurred; when 8 KJ·mol$^{-1} < E < 16$ KJ·mol^{-1}, the chemisorption occurred. When $E > 16$ KJ·mol^{-1}, the ion exchange occurred. It could be seen from Table 2 that E of the adsorption process of MB onto $Mg_{0.4}Co_{0.5}Zn_{0.1}Fe_2O_4$ nanoparticles was 0.2347 KJ·mol^{-1}, which was less than 8 KJ·mol^{-1}, indicating that physical adsorption existed in the adsorption process. In conclusion, physical and chemical adsorption both existed in the adsorption process of MB onto $Mg_{0.4}Co_{0.5}Zn_{0.1}Fe_2O_4$ nanoparticles [67].

Table 3 showed the maximum adsorption capacities of magnetic $Mg_{0.4}Co_{0.5}Zn_{0.1}Fe_2O_4$ nanoparticles and other adsorbents for MB. The adsorption capacity of MB adsorbed onto magnetic $Mg_{0.4}Co_{0.5}Zn_{0.1}Fe_2O_4$ nanoparticles was more than those of other adsorbents. The reason for the better adsorption capacity of magnetic $Mg_{0.4}Co_{0.5}Zn_{0.1}Fe_2O_4$ nanoparticles might be that magnetic $Mg_{0.4}Co_{0.5}Zn_{0.1}Fe_2O_4$ nanoparticles with positive charge may have electrostatic adsorption with MB and their surface was rich in hydroxyl groups. Moreover, magnetic $Mg_{0.4}Co_{0.5}Zn_{0.1}Fe_2O_4$ nanoparticles had the advantages of facile preparation and easy separation after adsorption with an external magnetic field, indicating that magnetic $Mg_{0.4}Co_{0.5}Zn_{0.1}Fe_2O_4$ nanoparticles had a wide application prospect in wastewater treatment.

3.3.3. Thermodynamic Study. The effect of MB solution temperature on the adsorption capacity of magnetic $Mg_{0.4}Co_{0.5}Zn_{0.1}Fe_2O_4$ nanoparticles was studied to verify the spontaneity of the process [68]. Equations (10)–(12) were used to calculate the thermodynamic parameters (ΔG^0, ΔH^0, and ΔS^0).

$$\ln K_0 = \frac{q_e}{C_e}, \tag{10}$$

$$\Delta G^0 = -RT \ln K_0, \tag{11}$$

$$\ln K_0 = -\frac{\Delta H^0}{RT} + \frac{\Delta S^0}{R}, \tag{12}$$

where K_0 was the distribution coefficient, R (8.314 J·mol^{-1}) was the gas constant, and K was the Kelvin temperature. The values of ΔH^0 and ΔS^0 were calculated using the slope and intercept of the $\ln K_0$ and $1/T$ curves. The relationship between $\ln K_0$ and $1/T$ was shown in Figure 6, and it was obvious that $\ln K_0$ had a good linear relationship with $1/T$. ΔG^0, ΔH^0, and ΔS^0 were shown in Table 4, and ΔH^0 was -10.38 KJ·mol^{-1}; the result showed that the adsorption of MB onto magnetic $Mg_{0.4}Co_{0.5}Zn_{0.1}Fe_2O_4$ nanoparticles was an exothermic process. ΔG^0 was less than 0 KJ·mol^{-1}, indicating that the process was a

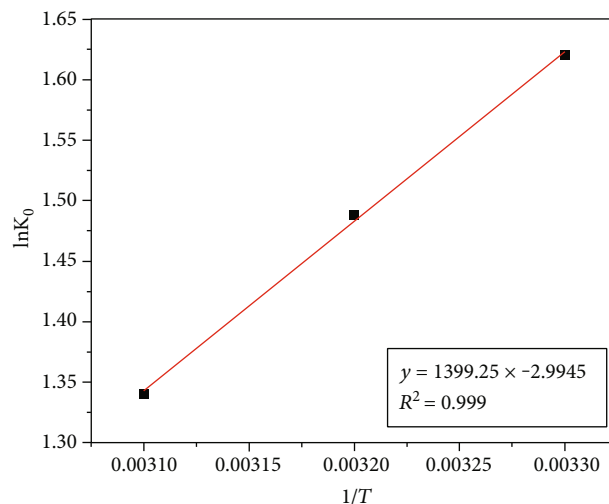
FIGURE 6: Adsorption thermodynamic of MB onto $Mg_{0.4}Co_{0.5}Zn_{0.1}Fe_2O_4$ nanoparticles at 303 K, 313 K, and 323 K.

TABLE 4: Thermodynamic parameters of MB adsorbed onto magnetic $Mg_{0.4}Co_{0.5}Zn_{0.1}Fe_2O_4$ nanoparticles.

T/K	ΔG^0/(KJ·Mol^{-1})	ΔH^0/(KJ·Mol^{-1})	ΔS^0/(J·mol^{-1}·K^{-1})
303	-4.08		
313	-3.87	-10.38	-20.80
323	-3.6		

K_0 was the distribution coefficient, R was the gas constant, and K was the Kelvin temperature. The values of ΔH^0 and ΔS^0 were calculated using the slope and intercept of the $\ln K_0$ and $1/T$ curves.
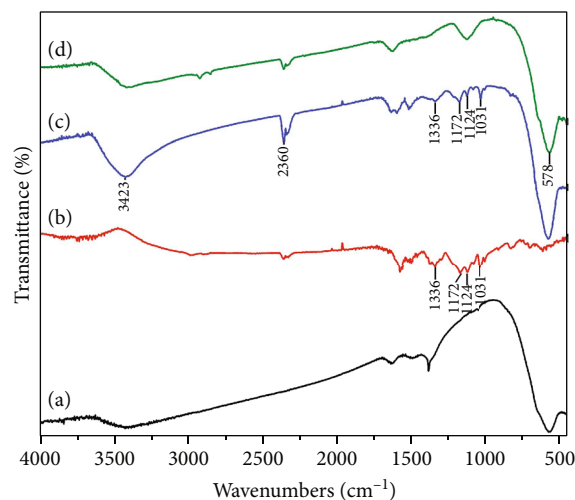
FIGURE 7: FTIR spectra of $Mg_{0.4}Co_{0.5}Zn_{0.1}Fe_2O_4$ nanoparticles (a), MB (b), magnetic $Mg_{0.4}Co_{0.5}Zn_{0.1}Fe_2O_4$ nanoparticles after adsorption (c), and magnetic $Mg_{0.4}Co_{0.5}Zn_{0.1}Fe_2O_4$ nanoparticle-adsorbed recalcination (d).

spontaneous reaction process. The thermodynamic experiment proved that the adsorption process of MB adsorbed onto magnetic $Mg_{0.4}Co_{0.5}Zn_{0.1}Fe_2O_4$ nanoparticles was a spontaneous exothermic reaction.

(a)

(b)

FIGURE 8: Effects of pH (a) on adsorption of MB onto magnetic $Mg_{0.4}Co_{0.5}Zn_{0.1}Fe_2O_4$ nanoparticles and recycling (b) of magnetic $Mg_{0.4}Co_{0.5}Zn_{0.1}Fe_2O_4$ nanoparticles calcined at 400°C for 2 h with 25 mL anhydrous ethanol.

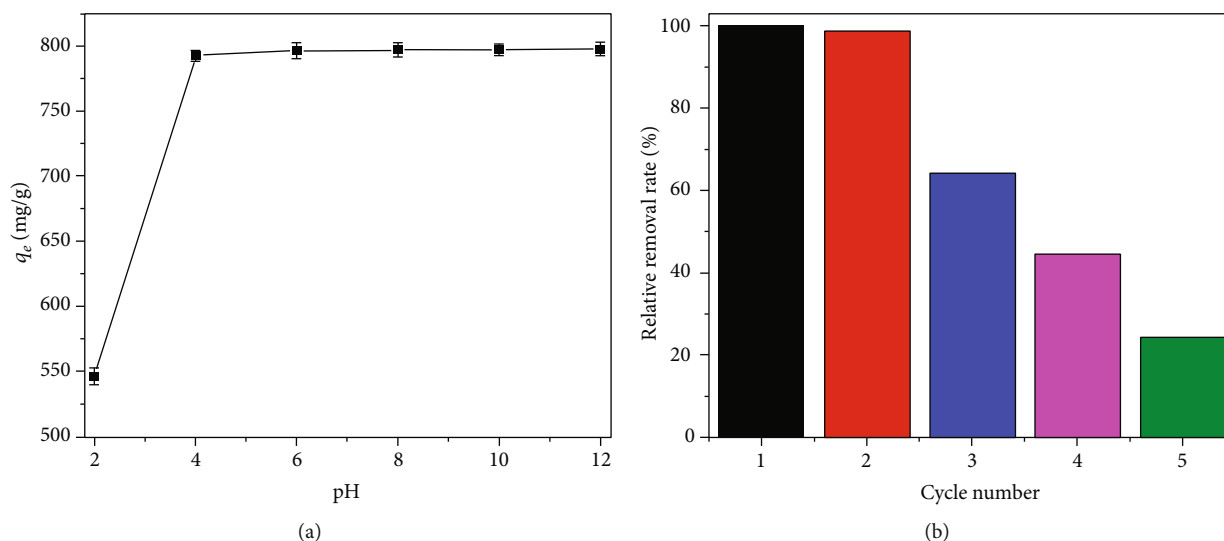## 3.4. Adsorption Mechanism of MB onto $Mg_{0.4}Co_{0.5}Zn_{0.1}Fe_2O_4$ Nanoparticles

3.4.1. FTIR Analysis.
The FTIR spectra of magnetic $Mg_{0.4}Co_{0.5}Zn_{0.1}Fe_2O_4$ nanoparticles, MB, magnetic $Mg_{0.4}Co_{0.5}Zn_{0.1}Fe_2O_4$ nanoparticles after adsorption, and magnetic $Mg_{0.4}Co_{0.5}Zn_{0.1}Fe_2O_4$ nanoparticle-adsorbed recalcination were shown in Figure 7. The Fe-O bond appeared at $578\,cm^{-1}$, the O-H bond appeared at $3423\,cm^{-1}$ which belonged to H_2O, and the $-SO_3Na$ bond appeared at $1031\,cm^{-1}$, indicating that MB was adsorbed onto magnetic $Mg_{0.4}Co_{0.5}Zn_{0.1}Fe_2O_4$ nanoparticles [1]. As shown in Figure 7 (D), after magnetic $Mg_{0.4}Co_{0.5}Zn_{0.1}Fe_2O_4$ nanoparticles were recalcined, most of the MB characteristic peaks disappeared, but the peak of $1124\,cm^{-1}$ appeared as a wide peak, indicating that MB was removed during the process of magnetic $Mg_{0.4}Co_{0.5}Zn_{0.1}Fe_2O_4$ nanoparticles recalcination and MB was adsorbed onto magnetic $Mg_{0.4}Co_{0.5}Zn_{0.1}Fe_2O_4$ nanoparticles utilizing chemical bonding. Hence, the calcined of magnetic $Mg_{0.4}Co_{0.5}Zn_{0.1}Fe_2O_4$ nanoparticles had an obvious adsorption effect and regeneration.

3.4.2. Influence of pH and Cycle Number.
The pH of the MB solution had a great influence on the adsorption capacity of magnetic $Mg_{0.4}Co_{0.5}Zn_{0.1}Fe_2O_4$ nanoparticles. Figure 8(a) showed that the adsorption capacity of magnetic $Mg_{0.4}Co_{0.5}Zn_{0.1}Fe_2O_4$ nanoparticles increased rapidly with the pH of MB increasing from 2 to 4. The adsorption capacity of magnetic $Mg_{0.4}Co_{0.5}Zn_{0.1}Fe_2O_4$ nanoparticles did not change significantly when the pH of MB increased from 4 to 12, and the saturated adsorption capacity of magnetic $Mg_{0.4}Co_{0.5}Zn_{0.1}Fe_2O_4$ nanoparticles increased from $792.42\,mg\cdot g^{-1}$ to $797.73\,mg\cdot g^{-1}$. The reason was that the isoelectric point of MB was 4. MB and the magnetic $Mg_{0.4}Co_{0.5}Zn_{0.1}Fe_2O_4$ nanoparticles of the surface had a positive charge, and when pH was less than 4, with the pH increasing, the positive charge on the surface of MB

decreased gradually, and the adsorption capacity gradually increased. The number of negative charges of MB was equal to the positive charges of magnetic $Mg_{0.4}Co_{0.5}Zn_{0.1}Fe_2O_4$ nanoparticles when the pH of MB solution was in 4-12, and the applied force between MB and magnetic $Mg_{0.4}Co_{0.5}Zn_{0.1}Fe_2O_4$ nanoparticles canceled out.

Cycle number was an important index to evaluate an adsorbent. Common regeneration methods included calcination regeneration, chemical regeneration, and biological regeneration. The retention of chemical solvents on the adsorbent and the residual of biological intermediates on the adsorbent would hinder the adsorption of pollutants on the adsorbent in subsequent cycles, and the regeneration efficiency would be significantly reduced after multiple cycles [69]. In contrast, the calcination method was the most widely used and the most mature regeneration method with simple operation and high regeneration efficiency. Therefore, the regeneration of $Mg_{0.4}Co_{0.5}Zn_{0.1}Fe_2O_4$ nanoparticles adsorbing MB was completed by calcination.

Figure 8(b) showed that the removal rate of magnetic $Mg_{0.4}Co_{0.5}Zn_{0.1}Fe_2O_4$ nanoparticles could still reach 98.75% of the first after 2 cycles. But the removal rate decreased significantly after 3 cycles, only 64.17% of the first. The reason was that with the cycle number increasing, the number of calcinations increased, and the collapse of adsorption voids of magnetic $Mg_{0.4}Co_{0.5}Zn_{0.1}Fe_2O_4$ nanoparticles resulted in the decrease of specific surface area; the adsorption sites decreased, and the adsorption effect deteriorated. The result suggested that magnetic $Mg_{0.4}Co_{0.5}Zn_{0.1}Fe_2O_4$ nanoparticles had good reusability.

The characterization of the recycled $Mg_{0.4}Co_{0.5}Zn_{0.1}Fe_2O_4$ nanoparticles after calcination was shown in Figure 9. According to Figure 9(a), compared to fresh $Mg_{0.4}Co_{0.5}Zn_{0.1}Fe_2O_4$ nanoparticles, the XRD of calcined nanoparticles had lower diffraction peaks. It could be seen from Figures 9(a) and 9(c) that the morphology of
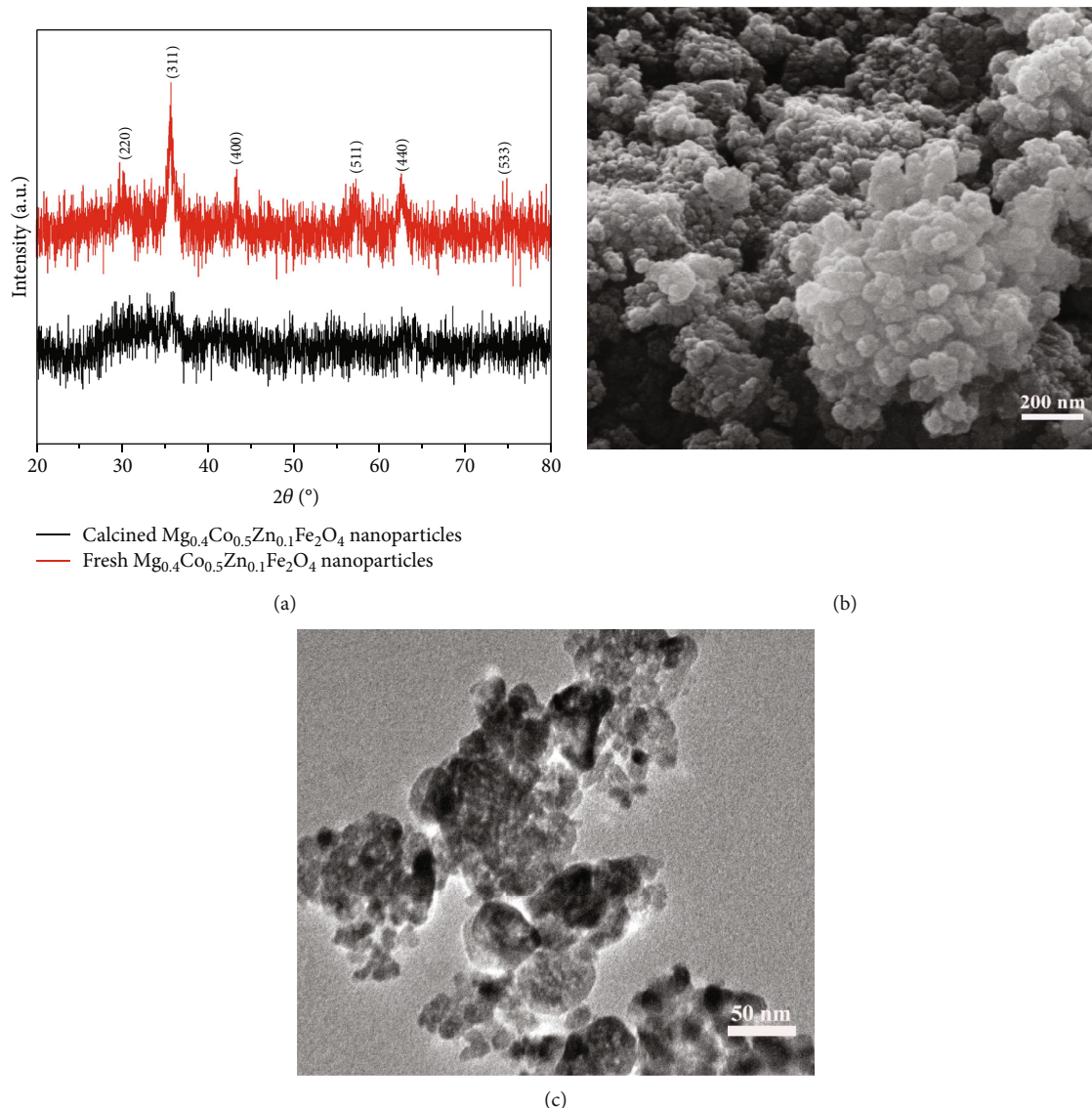
(a)

(b)

--- Calcined $Mg_{0.4}Co_{0.5}Zn_{0.1}Fe_2O_4$ nanoparticles
--- Fresh $Mg_{0.4}Co_{0.5}Zn_{0.1}Fe_2O_4$ nanoparticles

(c)

FIGURE 9: XRD (a), SEM (b), and TEM (c) of calcined $Mg_{0.4}Co_{0.5}Zn_{0.1}Fe_2O_4$ nanoparticles.

calcined $Mg_{0.4}Co_{0.5}Zn_{0.1}Fe_2O_4$ nanoparticles had not changed obviously. All these characterizations indicated that $Mg_{0.4}Co_{0.5}Zn_{0.1}Fe_2O_4$ nanoparticles had excellent cyclic properties.

3.4.3. Electrochemical of MB onto Magnetic $Mg_{0.4}Co_{0.5}Zn_{0.1}Fe_2O_4$ Nanoparticles. CV was used to investigate the change of electrical signals interacting with magnetic $Mg_{0.4}Co_{0.5}Zn_{0.1}Fe_2O_4$ nanoparticles. The CV curves of bare MGCE, MGCE/$Mg_{0.4}Co_{0.5}Zn_{0.1}Fe_2O_4$, and MGCE/$Mg_{0.4}Co_{0.5}Zn_{0.1}Fe_2O_4$/MB scanned between -0.1 V and 0.7 V were shown in Figure 10(a). The peak value of current decreased significantly when magnetic $Mg_{0.4}Co_{0.5}Zn_{0.1}$-Fe_2O_4 nanoparticles were added to the electrode, and the reason was that magnetic $Mg_{0.4}Co_{0.5}Zn_{0.1}Fe_2O_4$ nanoparticles obstructed the flow of $[Fe(CN)_6]^{3-/4-}$ to the surface of the electrode. The peak value of current was further reduced when magnetic $Mg_{0.4}Co_{0.5}Zn_{0.1}Fe_2O_4$ nanoparti-

cles adsorbing MB were added to the electrode, and the reason was that the interaction between MB and magnetic $Mg_{0.4}Co_{0.5}Zn_{0.1}Fe_2O_4$ nanoparticles further obstructed the flow of $[Fe(CN)_6]^{3-/4-}$ to the surface of the electrode.

EIS was a method to study charge transfer characteristics at the electrode interface. The Nyquist plot was a semicircular curve not centered on the real axis, and this kind of decentralization belonged to the non-Debye type relaxation process [70]. The Nyquist plot of bare MGCE (a), MGCE/$Mg_{0.4}Co_{0.5}Zn_{0.1}Fe_2O_4$ (b), and MGCE/$Mg_{0.4}Co_{0.5}Zn_{0.1}$-Fe_2O_4/MB (c) was shown in Figure 10(b). The size of the sample resistance was determined by the diameter of the semicircle. Magnetic $Mg_{0.4}Co_{0.5}Zn_{0.1}Fe_2O_4$ nanoparticle suspension was dropped onto the bare electrode, and the radius of the curve increased after magnetic $Mg_{0.4}Co_{0.5}Zn_{0.1}Fe_2O_4$ nanoparticles were added to the electrode. Comparing Figure 10(b) C with Figure 10(b) B, the radius of the circle

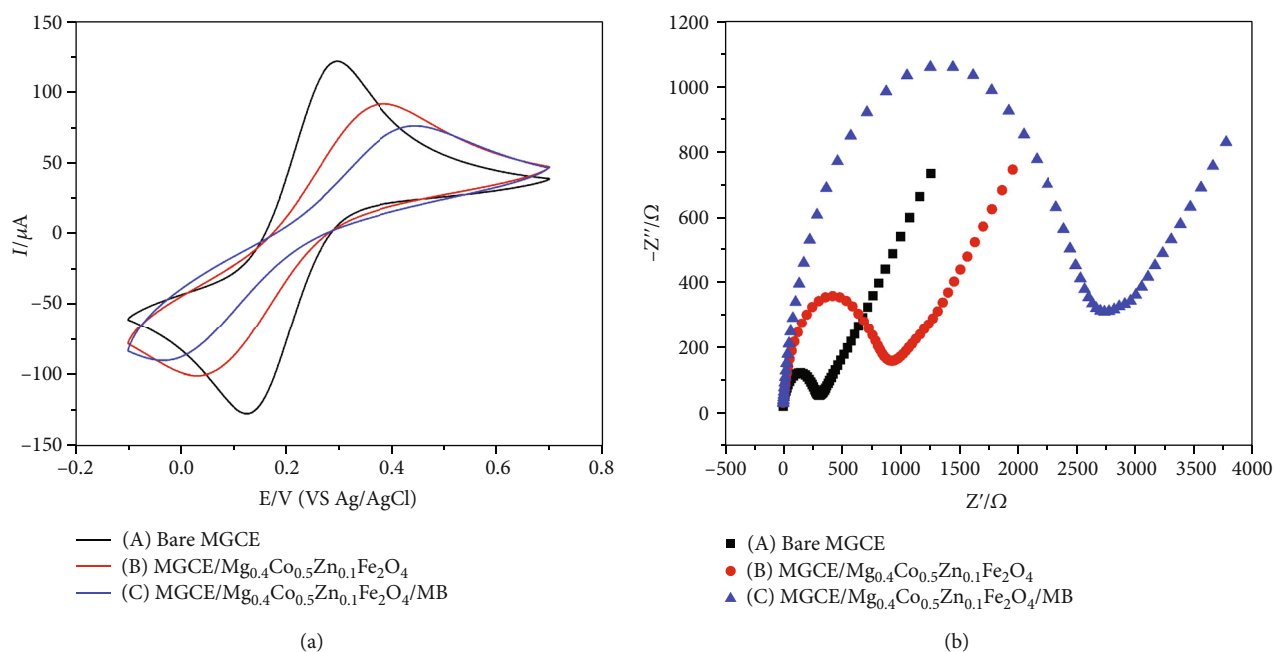(a)   (b)

FIGURE 10: The CV curves (a) and EIS curves (b) of bare MGCE (A), MGCE/$Mg_{0.4}Co_{0.5}Zn_{0.1}Fe_2O_4$ (B), and MGCE/$Mg_{0.4}Co_{0.5}Zn_{0.1}Fe_2O_4$/MB (C).

increased further. The results indicated that MB adsorbed onto magnetic $Mg_{0.4}Co_{0.5}Zn_{0.1}Fe_2O_4$ nanoparticles further increased the resistance. The electrochemical analysis further verified that MB was adsorbed onto magnetic $Mg_{0.4}Co_{0.5}Zn_{0.1}Fe_2O_4$ nanoparticles.

4. Conclusion

(1) Magnetic $Mg_{0.4}Co_{0.5}Zn_{0.1}Fe_2O_4$ nanoparticles were successfully prepared by the rapid combustion approach. The average particle size and the magnetic saturation intensity of the nanoparticles calcined at 400°C for 2 h with 25 mL anhydrous ethanol were 81.28 nm and 13.5 emu·g^{-1}, respectively

(2) The adsorption of MB onto $Mg_{0.4}Co_{0.5}Zn_{0.1}Fe_2O_4$ nanoparticles conformed to the pseudo-second-order model and Freundlich model, indicating that the adsorption process was a chemical multilayer adsorption mechanism. The D-R model indicated that the adsorption involved physical adsorption. Adsorption thermodynamics and the Temkin model demonstrated that the adsorption process was a spontaneous exothermic reaction

(3) The adsorption capacity of magnetic $Mg_{0.4}Co_{0.5}Zn_{0.1}Fe_2O_4$ nanoparticles reached 792.42 mg·g^{-1} when pH was 4, and the removal rate of magnetic $Mg_{0.4}Co_{0.5}Zn_{0.1}Fe_2O_4$ nanoparticles could still reach 98.75% of the first after 2 cycles, indicating that magnetic $Mg_{0.4}Co_{0.5}Zn_{0.1}Fe_2O_4$ nanoparticles had good application value

Data Availability

The research data used to support the finding of this study are included within the article.

Conflicts of Interest

The authors declare that they have no known competing financial interests or personal relationships that could have appeared to influence the work reported in this paper.

Supplementary Materials

Supplementary data associated with this article can be found in the online version (Supplementary Materials). *(Supplementary Materials)*

References

[1] S. Xie, Y. Yang, W. Z. Gai, and Z. Y. Deng, "Oxide modified aluminum for removal of methyl orange and methyl blue in aqueous solution," *RSC Advances*, vol. 11, no. 2, pp. 867–875, 2021.

[2] Y. Q. Hu, C. Hou, J. An et al., "Fe_3O_4-doped silk fibroin-polyacrylamide hydrogel for selective and highly efficient absorption of cationic dyes pollution in water," *Nanotechnology*, vol. 33, no. 26, article 265601, 2022.

[3] A. Ghedjemis, R. Ayeche, M. Kebaili, A. Benouadah, and L. F. Gil, "Application of natural hydroxyapatite in the treatment of polluted water: utilization of dromedary bone as bioadsorbent," *International Journal of Applied Ceramic Technology*, vol. 19, no. 4, pp. 2124–2134, 2022.

[4] Q. Shu, W. Qiu, M. Luo, and L. Xiao, "Morphology-controlled hydrothermal synthesis of copper selenides with orange juice

for highly efficient cationic dyes adsorption," *Materials Today Sustainability*, vol. 17, article 100094, 2022.

[5] B. Hayati, N. M. Mahmoodi, M. Arami, and F. Mazaheri, "Dye removal from colored textile wastewater by poly(propylene imine) dendrimer: operational parameters and isotherm studies," *Clean: Soil, Air, Water*, vol. 39, no. 7, pp. 673–679, 2011.

[6] N. M. Mahmoodi, M. Ghezelbash, M. Shabanian, F. Aryanasab, and M. R. Saeb, "Efficient removal of cationic dyes from colored wastewaters by dithiocarbamate-functionalized graphene oxide nanosheets: from synthesis to detailed kinetics studies," *Journal of the Taiwan Institute of Chemical Engineers*, vol. 81, pp. 239–246, 2017.

[7] Q. J. Chen, Y. L. Zhao, Q. H. Xie, C. Y. Liang, and Z. Y. Zong, "Polyethyleneimine grafted starch nanocrystals as a novel biosorbent for efficient removal of methyl blue dye," *Carbohydrate Polymers*, vol. 273, article 118579, 2021.

[8] J. W. Heo, L. L. An, J. S. Chen, J. H. Bae, and Y. S. Kim, "Preparation of amine-functionalized lignins for the selective adsorption of methylene blue and Congo red," *Chemosphere*, vol. 295, article 133815, 2022.

[9] M. A. Nazir, T. Najam, M. S. Bashir et al., "Kinetics, "isothermal and mechanistic insight into the adsorption of eosin yellow and malachite green from water via tri-metallic layered double hydroxide nanosheets"," *Korean Journal of Chemical Engineering*, vol. 39, no. 1, pp. 216–226, 2022.

[10] S. R. Mousavi, M. Asghari, and N. M. Mahmoodi, "Chitosan-wrapped multiwalled carbon nanotube as filler within PEBA thin film nanocomposite (TFN) membrane to improve dye removal," *Carbohydrate Polymers*, vol. 237, article 116128, 2020.

[11] P. Moradihamedani, "Recent advances in dye removal from wastewater by membrane technology: a review," *Polymer Bulletin*, vol. 79, no. 4, pp. 2603–2631, 2022.

[12] H. Zhang, M. Xu, M. N. Chen et al., "Fabrication of high flux porphrin-cored with siloxane-poly(amido amine) dendrimer/ PVDF composite membrane for oil/water separation and dye degradation," *Journal of Environmental Chemical Engineering*, vol. 10, no. 3, article 107634, 2022.

[13] J. C. Gu, T. Y. Chen, P. Xiao et al., "Constructing oxidized carbon spheres-based heterogeneous membrane with high surface energy for energy-free water purification," *Chemical Engineering Journal*, vol. 431, article 134132, 2022.

[14] H. S. Mona, J. Fattaneh, and D. Abdulhamid, "The study of TiO_2/Cu_2O nanoparticles as an efficient nanophotocalyst toward surface adsorption and photocatalytic degradation of methylene blue," *Applied Nanoscience*, vol. 12, no. 7, pp. 2195–2205, 2022.

[15] Z. H. Y. S. L. Zhu, L. H. Zhang, and S. Watanabe, "Mesoporous single crystal titanium oxide microparticles for enhanced visible light photodegradation," *Optical Materials*, vol. 127, article 112297, 2022.

[16] K. S. Hirpara and U. D. Patel, "Quantitative structure-activity relationship (QSAR) models for color and COD removal for some dyes subjected to electrochemical oxidation," *Environmental Technology*, vol. 43, pp. 1–12, 2022.

[17] J. Hou, X. Li, Y. T. Yan, and L. Z. Wang, "Electrochemical oxidation of methyl orange in an active carbon packed electrode reactor (ACPER): degradation performance and kinetic simulation," *International Journal of Environmental Research and Public Health*, vol. 19, no. 8, p. 4775, 2022.

[18] M. Mahreni, R. R. Ramadhan, M. F. Pramadhana, A. P. Permatasari, D. Kurniawati, and H. S. Kusuma, "Synthesis of metal organic framework (MOF) based Ca-alginate for adsorption of malachite green dye," *Polymer Bulletin*, vol. 79, no. 12, pp. 11301–11315, 2022.

[19] N. M. Mahmoodi, M. Oveisi, M. Bakhtiari et al., "Environmentally friendly ultrasound-assisted synthesis of magnetic zeolitic imidazolate framework - graphene oxide nanocomposites and pollutant removal from water," *Journal of Molecular Liquids*, vol. 282, pp. 115–130, 2019.

[20] Y. F. Liu, Y. Y. Shi, Y. Cui, F. Zhao, and M. D. Chen, "Design and preparation of imidazole ionic liquid-based magnetic polymers and its adsorption on sunset yellow dye," *Materials*, vol. 15, no. 7, p. 2628, 2022.

[21] H. Yang, Y. Sun, Q. Zhang et al., "$ZrMO_X$ particles for enhanced removal of methyl orange from wastewater: preparation, characterization, and adsorption study," *Adsorption Science & Technology*, vol. 2022, article 9685352, pp. 1–11, 2022.

[22] A. Almasian, M. E. Olya, and N. M. Mahmoodi, "Preparation and adsorption behavior of diethylenetriamine/polyacrylonitrile composite nanofibers for a direct dye removal," *Fibers and Polymers*, vol. 16, no. 9, pp. 1925–1934, 2015.

[23] E. M. Bakhsh, M. Bilal, M. Ali et al., "Synthesis of activated carbon from Trachycarpus fortunei seeds for the removal of cationic and anionic dyes," *Materials*, vol. 15, no. 6, p. 1986, 2022.

[24] A. A. Chirsty and P. Sivarukshy, "Comparison of adsorption properties of commercial silica and rice husk ash (RHA) silica: a study by NIR spectroscopy," *Open Chemistry*, vol. 19, no. 1, pp. 426–431, 2021.

[25] G. Y. Duan, Z. F. Cao, H. Zhong, X. Ma, and S. Wang, "Highly efficient poly(6-acryloylamino-N-hydroxyhexanamide) resin for adsorption of heavy metal ions," *Journal of Environmental Management*, vol. 308, article 114631, 2022.

[26] H. I. Lee and P. S. Lee, "Zeolite adsorbents for the separation of n-butyric acid from fermentation broths via adsorption," *Microporous and Mesoporous Materials*, vol. 334, article 111768, 2022.

[27] M. Mahinroosta and A. Allahverdi, "Pilot-scale valorization of hazardous aluminum dross into γ-Al2O3 nanoadsorbent for efficient removal of fluoride," *Environmental Technology and Innovation*, vol. 23, article 101549, 2021.

[28] L. M. Sanchez, E. Espinosa, P. M. Zelis, R. M. Martín, J. D. H. Niza, and A. Rodríguez, "Cellulose nanofibers/PVA blend polymeric beads containing *in-situ* prepared magnetic nanorods as dye pollutants adsorbents," *International Journal of Biological Macromolecules*, vol. 209, no. Part A, pp. 1211–1221, 2022.

[29] F. M. Alzahrani, N. S. Alsaiari, K. M. Katubi, A. Amari, F. B. Rebah, and M. A. Tahoon, "Synthesis of polymer-based magnetic nanocomposite for multi-pollutants removal from water," *Polymers*, vol. 13, no. 11, p. 1742, 2021.

[30] R. Janani, B. Gurunathan, K. Sivakumar, S. Varjani, H. H. Ngo, and E. Gnansounou, "Advancements in heavy metals removal from effluents employing nano-adsorbents: way towards cleaner production," *Environmental Research*, vol. 203, article 111815, 2022.

[31] M. Li, S. P. Kuang, Y. Kang, H. Q. Ma, J. H. Dong, and Z. Z. Guo, "Recent advances in application of iron-manganese oxide nanomaterials for removal of heavy metals in the aquatic environment," *Science of the Total Environment*, vol. 819, article 153157, 2022.

[32] Y. Mao, Y. Li, Z. H. Guo et al., "The coprecipitation formation study of iron oxide nanoparticles with the assist of a gas/liquid mixed phase fluidic reactor," *Colloids and Surfaces A: Physicochemical and Engineering Aspects*, vol. 647, article 129107, 2022.

[33] M. P. Moreira and D. Grasseschi, "Automation of a low-cost device for flow synthesis of iron oxide nanoparticles," *Journal of Nanoparticle Research*, vol. 24, no. 5, p. 93, 2022.

[34] C. N. Pinotti, L. M. D. Souza, W. P. Marques et al., "A new magnetic composite with potential application in boron adsorption: development, characterization, and removal tests," *Materials Chemistry and Physics*, vol. 277, article 125368, 2022.

[35] J. H. Chen, Z. Wang, and Z. X. Lv, "Adsorption of reactive red 2BF onto $Ni_{0.3}Co_{0.2}Zn_{0.5}Fe_2O_4$ nanoparticles fabricated via the ethanol solution of nitrate combustion process," *Materials Research Express*, vol. 8, no. 1, article 015006, 2021.

[36] W. S. Mohamed, N. M. A. Hadia, B. A. Bakheet, M. Alzaid, and A. M. Abu-Dief, "Impact of Cu^{2+} cations substitution on structural, morphological, optical and magnetic properties of $Co_{1-x}Cu_xFe_2O_4$ nanoparticles synthesized by a facile hydrothermal approach," *Solid State Sciences*, vol. 125, article 106841, 2022.

[37] M. Ni, J. Wang, J. Ma et al., "Synthesis of yttria nanopowder with poly acrylic acid as dispersant for highly transparent yttria ceramics," *Journal of the American Ceramic Society*, vol. 105, no. 3, pp. 2029–2037, 2022.

[38] J. T. Liu, Z. X. Luo, J. X. Yang et al., "Synthesis of non-agglomerating submicron/nano-$Yb_2Si_2O_7$ powders by a carbon-coated coprecipitation method," *Journal of the American Ceramic Society*, vol. 105, no. 9, pp. 5548–5554, 2022.

[39] C. Murugesan, L. Okrasa, K. Ugendar et al., "Improved magnetic and electrical properties of Zn substituted nanocrystalline $MgFe_2O_4$ ferrite," *Journal of Magnetism and Magnetic Materials*, vol. 550, article 169066, 2022.

[40] B. Yalcin, S. Ozcelik, K. Icin, K. Senturk, B. Ozcelik, and L. Arda, "Structural, optical, magnetic, photocatalytic activity and related biological effects of $CoFe_2O_4$ ferrite nanoparticles," *Journal of Materials Science: Materials in Electronics*, vol. 32, no. 10, pp. 13068–13080, 2021.

[41] M. P. Dojcinovic, Z. Z. Vasiljevic, V. P. Pavlovic et al., "Mixed Mg-Co spinel ferrites: structure, morphology, magnetic and photocatalytic properties," *Journal of Alloys and Compounds*, vol. 855, article 157429, 2021.

[42] C. M. Magdalane, G. M. A. Priyadharsini, K. Kaviyarasu, A. IrudayaJothi, and G. G. Simiyon, "Synthesis and characterization of TiO_2 doped cobalt ferrite nanoparticles via microwave method: investigation of photocatalytic performance of Congo red degradation dye," *Surfaces and Interfaces*, vol. 25, article 101296, 2021.

[43] J. C. R. Araújo, S. Araujo-Barbosa, A. L. R. Souza et al., "Tuning structural, magnetic, electrical, and dielectric properties of $MgFe_2O_4$ synthesized by sol-gel followed by heat treatment," *Journal of Physics and Chemistry of Solids*, vol. 154, article 110051, 2021.

[44] Z. Alsayed, M. S. Badawi, and R. Awad, "Investigation of thermal and mechanical behavior of $HDPE/ZnFe_2O_4$ composite," *Journal of Inorganic and Organometallic Polymers and Materials*, vol. 31, no. 7, pp. 2757–2765, 2021.

[45] Y. He, H. F. Tian, A. M. Xiang, S. B. Ma, D. Y. Yin, and A. V. Rajulu, "Fabrication of PVA/GO nanofiber films by electrospinning: application for the adsorption of Cu^{2+} and organic dyes," *Journal of Polymers and the Environment*, vol. 30, no. 7, pp. 2964–2975, 2022.

[46] Z. K. Heiba, M. A. Deyab, and A. M. El-naggar, "Electrochemical performance of quaternary $(1-x)ZnMn_2O_4/(x)MgFe_2O_4$ solid solution as supercapacitor electrode," *Ceramics International*, vol. 47, no. 6, pp. 7475–7486, 2021.

[47] S. Dabas, M. Chahar, and O. P. Thakur, "Electromagnetic interference shielding properties of $CoFe_2O_4$/polyaniline/poly(vinylidene fluoride) nanocomposites," *Materials Chemistry and Physics*, vol. 278, article 125579, 2022.

[48] L. Fei, F. Ali, A. Said et al., "Surface-functionalized spongy zinc ferrite as a robust visible-light driven nanocatalyst for wastewater remediation: characterization, kinetic, and mechanistic insight," *International journal of Environmental Science and Technology*, vol. 20, no. 1, pp. 1007–1018, 2023.

[49] D. C. Nguyen, C. C. Chu, A. K. Anbalagan, C. H. Lee, and C. S. Chang, "Rietveld refinement and X-ray absorption study on the bonding states of lanthanum-based perovskite-type oxides $La_{1-x}Ce_xCoO_3$," *Crystals*, vol. 12, no. 1, p. 50, 2022.

[50] P. Gupta, K. Kumar, S. H. Saeed et al., "Influence of tin doping on the liquefied petroleum gas and humidity sensing properties of NiO nanoparticles," *Journal of Materials Research*, vol. 37, no. 1, pp. 369–379, 2022.

[51] P. Chitra, E. R. Kumar, T. Pushpagiri, and A. Steephen, "Size and phase purity-dependent microstructural and magnetic properties of spinel ferrite nanoparticles," *Journal of Superconductivity and Novel Magnetism*, vol. 34, no. 4, pp. 1239–1244, 2021.

[52] M. A. Gabal and A. A. Al-Juaid, "Structural and electromagnetic studies of $Mg_{1-x}Zn_xFe_2O_4$ nanoparticles synthesized via a sucrose autocombustion route," *Journal of Materials Science: Materials in Electronics*, vol. 31, no. 13, pp. 10055–10071, 2020.

[53] N. Azouaou, H. Mokaddem, O. Allalou, N. Boudechiche, and Z. Sadaoui, "Synergistic effect of cafeterias and domestic wastes for the removal of lead from aqueous solution," *Reaction Kinetics, Mechanisms and Catalysis*, vol. 135, no. 1, pp. 403–424, 2022.

[54] B. S. Yadav and S. Dasgupta, "Effect of time, pH, and temperature on kinetics for adsorption of methyl orange dye into the modified nitrate intercalated MgAl LDH adsorbent," *Inorganic Chemistry Communications*, vol. 137, article 109203, 2022.

[55] N. Hassan, A. Shahat, I. M. El-Deen, M. A. M. El-Afify, and M. A. El-Bindary, "Synthesis and characterization of NH_2-MIL-88(Fe) for efficient adsorption of dyes," *Journal of Molecular Structure*, vol. 1258, article 132662, 2022.

[56] J. Yu, X. D. Li, M. Wu et al., "Synergistic role of inherent calcium and iron minerals in paper mill sludge biochar for phosphate adsorption," *Science of the Total Environment*, vol. 834, article 155193, 2022.

[57] D. Balarak, M. Zafariyan, C. A. Igwegbe, K. K. Onyechi, and J. O. Ighalo, "Adsorption of acid blue 92 dye from aqueous solutions by single-walled carbon nanotubes: isothermal, kinetic, and thermodynamic studies," *Environmental Processes*, vol. 8, no. 2, pp. 869–888, 2021.

[58] T. J. Al-Musawi, P. Rajiv, N. Mengelizadeh, I. A. Mohammed, and D. Balarak, "Development of sonophotocatalytic process for degradation of acid orange 7 dye by using titanium dioxide nanoparticles/graphene oxide nanocomposite as a catalyst," *Journal of Environmental Management*, vol. 292, article 112777, 2021.

[59] Q. Guo, Y. Zhao, G. S. Qi, and Y. Z. Liu, "Performance and mechanism of gas-solid adsorption in a rotating adsorption bed," *Chemical Engineering and Technology*, vol. 45, no. 5, pp. 844–852, 2022.

[60] A. A. Almethen, K. M. Alotaibi, H. S. Alhumud, and A. M. Als-wieleh, "Highly efficient and rapid removal of methylene blue from aqueous solution using folic acid-conjugated dendritic mesoporous silica nanoparticles," *PRO*, vol. 10, no. 4, p. 705, 2022.

[61] R. T. Kapoor, M. Rafatullah, M. R. Siddiqui, M. A. Khan, and M. Sillanpää, "Removal of reactive black 5 dye by banana peel biochar and evaluation of its phytotoxicity on tomato," *Sustainability*, vol. 14, no. 7, p. 4176, 2022.

[62] R. T. Yin, S. S. Zhang, Y. Y. Xu, J. M. Xue, J. Q. Bi, and R. J. Liu, "Adsorption mechanism and electrochemical properties of methyl blue onto magnetic $Co_xCu_{(1-x)}Fe_2O_4$ nanoparticles prepared via an alcohol solution of nitrate combustion and calcination process," *Journal of Inorganic and Organometallic Polymers and Materials*, vol. 31, no. 8, pp. 3584–3594, 2021.

[63] M. Ghaly, M. R. Abass, and Z. A. Mekawy, "Performance of molybdenum vanadate loaded on bentonite for retention of cesium-134 from aqueous solutions," *Environmental Science and Pollution Research*, vol. 30, no. 21, pp. 60432–60446, 2023.

[64] O. M. Adedeji and K. Jahan, "Removal of pollutants from aqueous product of co-hydrothermal liquefaction: adsorption and isotherm studies," *Chemosphere*, vol. 321, article 138165, 2023.

[65] A. D. Khatibi, M. Yilmaz, A. H. Mahvi, D. Balarak, and S. Salehi, "Evaluation of surfactant-modified bentonite for acid red 88 dye adsorption in batch mode: kinetic, equilibrium, and thermodynamic studies," *Desalination and Water Treatment*, vol. 271, pp. 48–57, 2022.

[66] F. K. Mostafapour, A. H. Mahvi, A. D. Khatibi, M. K. Saloot, N. Mohammadzadeh, and D. Balarak, "Adsorption of lead(II) using bioadsorbent prepared from immobilized Gracilaria corticata algae: thermodynamics, kinetics and isotherm analysis," *Desalination and Water Treatment*, vol. 265, pp. 103–113, 2022.

[67] F. K. Mostafapour, M. Yilmaz, A. H. Mahvi, A. Younesi, F. Ganji, and D. Balarak, "Adsorptive removal of tetracycline from aqueous solution by surfactant-modified zeolite: equilibrium, kinetics and thermodynamics," *Desalination and Water Treatment*, vol. 247, pp. 216–228, 2022.

[68] F. M. Valadi, S. Shahsavari, E. Akbarzadeh, and M. R. Gholami, "Preparation of new MOF-808/chitosan composite for Cr(VI) adsorption from aqueous solution: experimental and DFT study," *Carbohydrate Polymers*, vol. 288, article 119383, 2022.

[69] X. Y. Ying, G. Kim, I. Han, J. Y. Sheng, Q. W. Mei, and Y. Kim, "High efficiency regeneration performance of exhausted activated carbon by superheated steam and comparison with conventional chemical regeneration method," *KSCE Journal of Civil Engineering*, vol. 26, no. 5, pp. 2058–2067, 2022.

[70] T. Dabbebi, S. Hcini, B. Alzahrani et al., "Investigations of microstructural and impedance spectroscopic properties of $Mg_{0.5}Co_{0.5}Fe_{1.6}Al_{0.4}O_4$ ferrite prepared using sol-gel method," *Journal of Materials Science: Materials in Electronics*, vol. 32, no. 9, pp. 12521–12534, 2021.

[71] Y. W. Shi, G. B. Song, A. Q. Li et al., "Graphene oxide-chitosan composite aerogel for adsorption of methyl orange and methylene blue: effect of pH in single and binary systems," *Colloids and Surfaces A: Physicochemical and Engineering Aspects*, vol. 641, article 128595, 2022.

[72] L. Yang, Y. F. Zhan, Y. J. Gong et al., "Development of eco-friendly CO_2-responsive cellulose nanofibril aerogels as "green" adsorbents for anionic dyes removal," *Journal of Hazardous Materials*, vol. 405, article 124194, 2021.

[73] Y. He, W. L. Bao, Y. C. Hua et al., "Efficient adsorption of methyl orange and methyl blue dyes by a novel triptycene-based hyper-crosslinked porous polymer," *RSC Advances*, vol. 12, no. 9, pp. 5587–5594, 2022.

[74] H. Deb, M. Z. Islam, A. Ahmed et al., "Kinetics & dynamic studies of dye adsorption by porous graphene nano-adsorbent for facile toxic wastewater remediation," *Journal of Water Process Engineering*, vol. 47, article 102818, 2022.